Journal of Hydrology 573 (2019) 180–193

Contents lists available at ScienceDirect

Journal of Hydrology

journal homepage: www.elsevier.com/locate/jhydrol

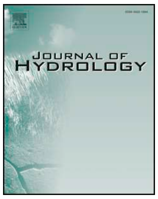

Research papers

Turbulence structure in open channel flow with partially covered artificial emergent vegetation

Wen-Xin Huai[a,*], Jiao Zhang[a], Wei-Jie Wang[b,c], Gabriel G. Katul[d,e]

[a] State Key Laboratory of Water Resources and Hydropower Engineering Science, Wuhan University, Wuhan, Hubei 430072, China
[b] State Key Laboratory of Simulation and Regulation of Water Cycle in River Basin, China Institute of Water Resources and Hydropower Research, Beijing 100038, China
[c] Department of Water Environment, China Institute of Water Resources and Hydropower Research, Beijing 100038, China
[d] Nicholas School of the Environment, Duke University, Durham, NC 27708, USA
[e] Department of Civil and Environmental Engineering, Duke University, Durham, NC 27708, USA

ARTICLE INFO

This manuscript was handled by G. Syme, Editor-in-Chief, with the assistance of Xiaodong Zhang, Associate Editor

Keywords:
Emergent artificial vegetation area
Flow resistance
Quadrant analysis
Spectral analysis
Turbulent structures

ABSTRACT

An innovative approach was recently proposed to increase water depth and improve navigation in rivers by increasing overall roughness through an adaptive placement of artificial vegetation. In this approach, a section of the river width is covered with artificial vegetation constructed from an array of dampers that can be added or removed while maintaining sufficient width for navigational purposes. The goal of the work here is to explore the mean flow and turbulent momentum transport properties of such flow in a controlled flume setting, where the flow rate is steady, the vegetation placement is uniform, and the Froude number is maintained at sub-critical conditions. The focus is on vegetation-induced roughness alterations to the bulk flow statistics as well as the structure of turbulence impacted by the presence of such artificially engineered vegetation. The canopy flow experimentally explored here differs from the well-studied planar uniform emergent canopy flow because the interface between the vegetation and non-vegetation areas occurs along a lateral direction instead of the vertical direction. The flume experiments were conducted by partially covering the channel width with emergent artificial vegetation that is flexible and can interact with the flow. The quantities studied are the equilibration distance of the flow statistics from the leading vegetation edge as such distance is essential to any engineering design. Moreover, the mean flow and turbulence regimes at several longitudinal sections were analyzed using spectral analysis and conditional sampling to identify the main vortical structures and their contribution to momentum transport. Spectral analysis demonstrated that the sizes of the dominant vortices can be classified into stem-scale (small-scale) and shear-scale (larger scale) vortices as conventional in canonical canopy flows. The shear layer formed in the planar direction and its associated coherent vortices are spawned near the edge of the vegetated area in a manner analogous to a plane mixing layer. Quadrant analysis showed two contributions to the overall shear stress and lateral momentum exchange between the vegetated and non-vegetated zone, namely, ejections and sweeps. The measured ejection-sweep contributions are short-lived but significant to the overall turbulent momentum transport consistent with other canopy flow studies. Approximately 80% of the turbulent stress contributions at the interface occur within 30% of the time. Because the flume experiments were conducted at sufficiently high Reynolds number and sufficiently low Froude number, the scalability of the experimental findings here to much larger settings encountered in engineering practice are briefly discussed.

1. Introduction

Resistance laws describing water movement in natural rivers covered by vegetation continue to draw research interest given their significance to a plethora of hydrological, ecological and engineering applications. Interest in flow within artificial vegetation is now moving from the margins of laboratory research to the utility in river management and operation. Zdankus et al. (2016) proposed that artificial vegetation can be used to control river flow and improve navigational depth by increasing resistance to flow. Their proposed artificial vegetation, which resembles colonies of water plants with long afloat culms, is environmentally friendly and convenient to construct or manufacture. The use of such artificial vegetation to increase resistance in rivers poses unique scientific challenges that require further inquiry

---

[*] Corresponding author.
E-mail address: wxhuai@whu.edu.cn (W.-X. Huai).

https://doi.org/10.1016/j.jhydrol.2019.03.071
Received 29 June 2018; Received in revised form 18 March 2019; Accepted 19 March 2019

using controlled experiments. To begin with, the aforementioned artificial vegetation is flexible, not rigid, its placement in rivers results in configurations that differ from the well-studied vegetation used in laboratory and field studies, and the links between geometric and drag properties of such artificial vegetation are far from being understood. Based on the artificial vegetation type proposed by Zdankus et al. (2016), flume experiments are performed here to progress on these aforementioned issues. The goal is to primarily explore the mean flow and turbulent structure within such artificial aquatic vegetation with a focus on momentum transport. Equilibration distance from the leading edge of the vegetation section where the mean longitudinal velocity gradients become small does set a minimum required vegetation length to be used in such river management. Conventional spectral and quadrant analyses are employed to determine sizes and lateral momentum exchange between the flow in vegetated and non-vegetated areas. The results here are then compared with published laboratory and numerical studies that use conventional aquatic vegetation. It is envisaged that the outcome of the experiments here can be used to develop the next generation of Reynolds-averaged Navier-Stokes (RANS) models and offer a bench-mark data set for testing Large-eddy simulations (LES) subgrid schemes for such vegetation configuration. On the topic of RANS, one of the main novelties here is a link between ejections and sweeps responsible for momentum transport, the vortical sizes identified by spectral analysis, and vertical gradients of the second-order flow statistics at a given location. This novelty provides a new perspective on the difficult to model flux-transport terms in momentum transport within and across interfaces.

2. Review of flow through aquatic vegetation

What distinguishes flow above and within aquatic vegetation from its well-studied terrestrial counterpart is the fact that aquatic vegetation can be emergent ($H < h_c$) or submerged ($H > h_c$) depending on the water depth (H) and vegetation height (h_c). The flow structure of the submerged vegetation is more complex than that of the emergent vegetation. Beyond these two obvious length scales (H, h_c), vegetation in natural rivers does complicate the flow structure above and beyond canonical rough-wall turbulent boundary layers by introducing additional length scales that depend on the drag force distribution within the vegetated elements, stem diameter, distance from the ground, among others (Katul et al., 2004; Dunn et al., 1996; Järvelä, 2005; Kubrak et al., 2008; Huai et al., 2018). It has been known that the mean velocity within vegetated areas is reduced due to the presence of distributed drag elements but remains finite. The slow flow within vegetated elements and the fast flow in the vegetation-free zone can lead to an inflection point in the mean velocity making canopy flows resemble plane-mixing layers (i.e. a free-shear flow) (Katul et al., 2002) instead of canonical turbulent boundary layers (i.e. a bounded flow) (Pope, 2000) as discussed elsewhere (Raupach et al., 1996; Ho and Huerre, 1984; Termini, 2015).

Most of the studies on flow within and above vegetated canopies considered rigid canopies. In the case of uniform flow for submerged dense rigid vegetation (e.g. rods), three layers have been identified (Poggi et al., 2004a; Ghisalberti and Nepf, 2009) along the vertical direction (z, with $z = 0$ being the channel bottom). The first layer, roughly for $z/h_c < 1/2$ is dominated by Karman streets behind a single vegetation element (rod) presumably due to the lower Reynolds number in this region. The second layer, roughly for $1/2 < z/h_c < 3/2$ is dominated by Kelvin-Helmholtz vortices produced through the aforementioned inflectional instability near the canopy interface $z/h_c = 1$ (at least when the vegetation is sufficiently dense). The third layer, roughly spanning $z/h_c > 3/2$, resemble canonical turbulent boundary layer flows attached to a zero-plane displacement (instead of a wall). The turbulent flow structures in the second layer have been examined through quadrant analysis in numerous laboratory and field studies. It was found that among the four types of momentum transfer mechanisms (outward and inward interactions, sweeps, and ejections), sweeps dominate momentum transport for dense canopies (Vivoni, 1998; Poggi et al, 2004b; Ghisalberti and Nepf, 2006; Maltese et al., 2007; Righetti, 2008; Nezu and Sanjou, 2009; Hopkinson, 2014) analogous to air flow above terrestrial vegetation (Raupach and Thom, 1981). This conceptual picture proved effective when modeling the mean velocity and turbulent stresses in 1-D uniform flow (along z) though its extension to other dimensions remains a topic of inquiry. In the case of dense emergent rigid vegetation covering the half width of a channel along the longitudinal direction (similar to the case to be studied here), White and Nepf (2007, 2008) found a coherent vortex structure occurring at the interface between vegetation and the bulk flow in the vegetation-free zone. The dominant frequency was determined using spectral analysis and the vortex development appears to be accompanied by ejections and sweeps that lead to mass and momentum exchanges between the canopy and non-canopy regions. Ghisalberti and Nepf (2006) also considered the flow through open channels partially covered by submerged rigid vegetation and found strong sweeps in the front part of the vortex with weak ejections appearing in the vortex tail.

Flow within and over flexible vegetation began to draw significant research attention given their ubiquitous presence in natural streams. Unsurprisingly, the flow above and within rigid and flexible vegetation was found to share some commonalities and differences. For submerged flexible vegetation, layered flow structure and K-H vortices can form over the top of a flexible canopy in response to the mean and turbulent flow field. However, in contrast to rigid vegetation, flexible vegetation (to be used here) bends or even oscillates when the flow enters a vegetated area (i.e. a drag reduction mechanism). With increased flow velocity, flexible vegetation occupies one of four states such as vertical, slight swinging, strong and periodic vibrating (monami phenomenon), and stationary leaning states (Murota et al., 1984). Experiments by Ghisalberti and Nepf (2002) showed that the vortex frequency, the strong vibration frequency of the longitudinal velocity, and the swing frequency of the vegetation (monami) are comparable. They also found that monami appeared when the vortex velocity significantly exceeded the mean velocity in the mixing layer. This emerging picture about the vortical structure of flow through aquatic vegetation provides the template for analyzing the flow to be studied here. To what extent the vortical structure and their contribution to momentum transport can be juxtapositioned to the setup here is explored using the flume experiments described next.

The aforementioned studies place the vegetation in a manner to cover the entire channel width and a substantial portion of the channel length. However, in the study here, the focus is on a channel partially covered by flexible vegetation, namely riparian systems. These systems are ubiquitous in nature and river-riparian vegetation interaction is a significant component of eco-hydraulics research. The flow structure induced by the emergent vegetation growing on the riverbank shares similar characteristics with the one induced by submerged vegetation covering the whole width of the flume. Both vegetation patterns cause vortex formation and mass transport between the vegetated and vegetation-free zone. However, there are differences between them worth highlighting. Flexible vegetation covering riverbanks is an active component of ecosystem dynamics that impact fluvial processes, mass and sediment transport, and river morphology on long time scales. In turn, the river provides water, nutrients, and seeds to riverbank vegetation, which depends on the hydraulic, hydrological, and geomorphological characteristic of the rivers (Allmendinger et al., 2005). Camporeale et al. (2013) studied the main interactions between rivers and vegetation on a riverbank and proposed a model demonstrating the importance of connecting fluvial morpho-dynamics and riparian vegetation dynamics. Due to turbulence induced by the bed and vegetated edge, the flow structure is significantly more complex in conditions with bankside vegetation than that with submerged vegetation. For submerged flexible vegetation on a riverbank, the horizontal and

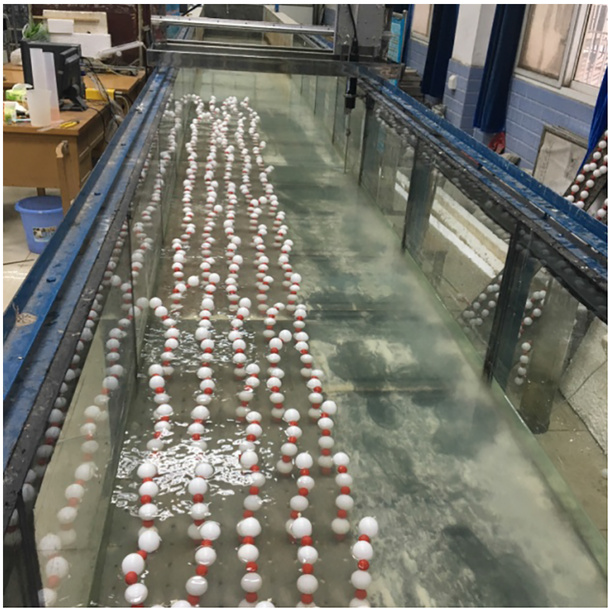

Fig. 1. Experimental setup showing the placement of the artificial vegetation in the flume.

vertical vortices occur at the interface between the main channel area and vegetation area, which enhance the mass and sediment transport between these two areas (Anderson et al. 2006). The turbulent shear (forming vortices) that transfer momentum away from the bed to the banks has been thoroughly investigated in several studies reviewed elsewhere (Rabkova and Garanina, 2001).

3. Experimental facility and conditions

The experiments were performed at the State Key Laboratory of Water Resources and Hydropower Engineering Science in Wuhan University using a 20 m long, 1 m wide (=B), and 0.4 m deep glass flume with a bed slope S_0 set to 0.01% (see Fig. 1). A steady uniform flow was obtained by adjusting the tailgate at the end of the flume. PVC (polyvinyl chloride) baseboards (2 m length × 0.25 m width × 0.01 m thickness) were used to cover half of B as shown in Fig. 1. An 8 m long section was partially covered with artificial vegetation (called dampers) starting from 6.5 m away from the water entrance into the flume. Dampers spanned about half of the flume width thereby making the vegetation domain $L_{veg} = 8$ m long and 0.495 m wide. The distance between two nearby vegetated elements in the longitudinal and transverse directions were 0.2 and 0.1 m, respectively.

The coordinate system used is as follows: The x-axis is aligned along the longitudinal direction, with x = 0 set at the leading edge of the vegetation domain. The y-axis is the transverse direction with $y = 0$ at the wall of the non-vegetated domain. The z-axis is the vertical direction as before with the flume bed set to $z = 0$ (see Fig. 2). Dampers were attached at the bottom of the flume by a thin rope and arranged in a parallel manner. The streamwise velocity distribution was measured using an Acoustic Doppler Velocimeter (ADV) with a sampling frequency of 50 Hz. The sampling time is 120 s for each measurement location resulting in 6000 samples per point. Measuring points were located at the mid-depth of the flow as proxies for the depth-averaged velocities, namely, $U \approx U_d$ (White and Nepf, 2007, 2008). The averaged relative errors between the depth averaged velocity and mid depth velocity taken at z = $H/2$ are below 10% for non-vegetated domain and below 15% for vegetated domain, where relative error for each measured point is calculated based on$|U_{dep} - U_{mid}|/U_{dep} * 100\%$, where U_{dep} is depth averaged velocity and U_{mid} is the velocity at z = $H/2$. These errors are larger than the ones reported by White and Nepf (2007, 2008) as the vegetation here has more complex form and swings. Given this small error, measuring the mid depth velocity and setting it to the depth average velocity is an acceptable approximation.

The form of artificial vegetation is different from previous laboratory vegetation studies. A single damper is constructed by four hollow floats and four solid floats. All dampers remain in a normal state with the forces of gravity and buoyancy (see Fig. 3). The diameters of the hollow and solid floats are 0.04 and 0.02 m, respectively.

The projection height of the damper changes with water depth H, and the damper extends from the bottom of the bed to the water surface. Therefore, the damper can be treated as the single emergent vegetation. Experiments here were carried out for three H values using such dampers as vegetation cover. The experimental arrangements and key flow statistics are summarized in Table 1, where Q is the discharge, F_r ($= U/\sqrt{gH}$) is a bulk Froude number, H is the water depth as before, n is the friction coefficient at the bottom of the channel determined based on the water depth and material type, S_o is the bed slope as before, Re ($= UH/\upsilon$, where υ is the water kinematic viscosity) is a bulk Reynolds number, and Re_d ($= Ud/\upsilon$, where d is arithmetic mean of float diameters) is a stem Reynolds number.

4. Results and discussions

The results and discussion sections are presented as follows. In section 4.1, the region where the mean flow and key eddy structures are in equilibrium with the vegetated section (i.e. minimal longitudinal gradients) is identified. The effective size of the region impacted by the presence of the vegetation is then delineated. Next, the turbulent energy content and the corresponding frequency of the dominant vortices is explored along the longitudinal and lateral distances in Section 4.2 with a focus on the equilibrated state away from the leading edge of the vegetation. The goal of section 4.2 is to identify whether a single or multi-scale vortices dominant the energy content of the measured velocity fluctuations. This analysis makes use of power-spectral density estimates on individual component-wise velocity time series. In Section 4.3, the lateral momentum transporting properties of eddies is explored using conventional quadrant analysis. The quadrant analysis is supplemented by a hyperbolic hole conditional sampling scheme to assess differential contributions of extreme momentum transporting events as a function of hyperbolic hole size. The duration and momentum contribution of coherent structures are determined for all three configurations listed in Table 1. Models that link ejection-sweep contributions to momentum transport are then explored.

The data and results in the figures are normalized using geometrical as well as flow variables. Unless otherwise stated, the longitudinal distances (or x) is normalized by the length of the vegetated strip (i.e. L_{veg}); transverse distances (or y) is normalized by the width of non-vegetated region b (=0.505 m) resulting in $0 < y/b < 1$ being the non-vegetated area, and $1 < y/b < 2$ being vegetated area; velocities are normalized by the time and area-averaged velocity ($U_m = Q/(BH)$), and Reynolds stresses are normalized by a bulk friction velocity given by $u_{*b} = \sqrt{gR_H S_o}$, where $R_H = \frac{BH}{B+2H}$ is the hydraulic radius defined here based on the bulk area (B*H) and wetted perimeter ($B + 2H$) in the absence of vegetation. While other normalizations that consider explicitly the vegetation are possible, the one selected here is in keeping with bulk flow variables used in conventional open channel flow studies.

4.1. Mean flow and turbulence characteristics

Fig. 4 presents the measured transverse distributions of the streamwise velocity (U_d) and the development of the mixing layer with increasing distance x. The measured spatial evolution of the streamwise mean velocity is normalized by the measured bulk mean velocity U_m as earlier noted. The mixing layer appears to be contained within the width of two inflection points (y_1, y_2) noted in the mean velocity

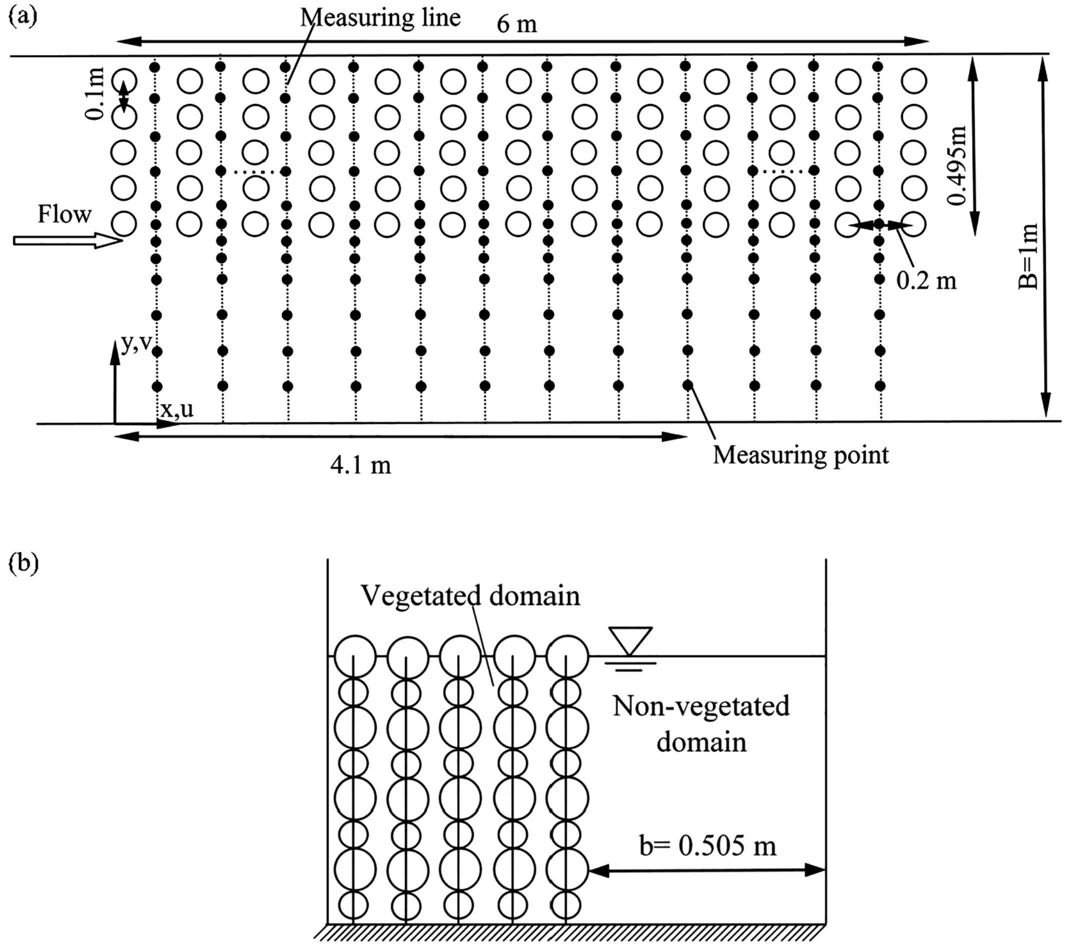

Fig. 2. Arrangement of the vegetated section: (a) plan view and (b) side view. B is the width of the channel in plan view (a) and b$\approx B/2$ is the width of the non-vegetated section. The hollow circles in the plan and side view represent the dampers, and the small dots represent the locations where ADV measurements were made.

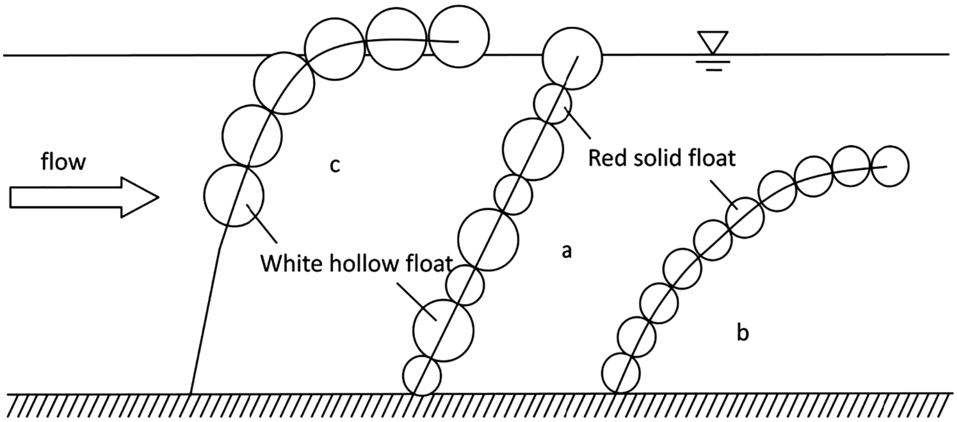

Fig. 3. A damper in the normal state adopted in the experiments here (a), with prevailing forces of gravity (b) and buoyancy (c).

Table 1
Flow parameters for the experimental conditions spanning the three water level cases.

Cases	Vegetation layout	Q (m^3/s)	F_r	H (m)	n	S_0	Re ($\times 10^4$)	Re_d ($\times 10^3$)
1	Asymmetric cover	0.02	0.164	0.115	0.009	0.001	2.0	2.6
2	Asymmetric cover	0.03	0.165	0.15	0.009	0.001	3.0	2.7
3	Asymmetric cover	0.05	0.172	0.205	0.009	0.001	4.7	3.0

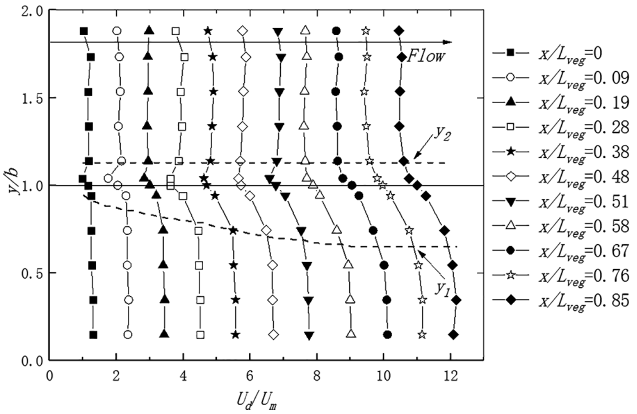

Fig. 4. Transverse distribution of streamwise mean velocity with increasing distance from the beginning of the vegetation area for Case 2. The thickness of the mixing layer limits y_1 and y_2, is shown by dash lines. The thin solid line represents the interface between vegetated and non-vegetated areas. Position markers are $x/L_{veg} = 0$ (■), $x/L_{veg} = 0.09$ (○), $x/L_{veg} = 0.19$ (▲), $x/L_{veg} = 0.28$ (□), $x/L_{veg} = 0.38$ (★), $x/L_{veg} = 0.48$ (◊), $x/L_{veg} = 0.51$ (▼), $x/L_{veg} = 0.58$ (△), $x/L_{veg} = 0.67$ (●), $x/L_{veg} = 0.76$ (☆), and $x/L_{veg} = 0.85$ (◆).

distribution inside and outside vegetated areas.

A strictly uniform transverse distribution of mean velocity cannot be expected just before and when the flow first encounters the artificial vegetation ($x = 0$) due to upstream pressure effects originating from the blockage caused by the vegetation elements. Following the leading edge ($x > 0$), an adjustment region is formed that links the upstream conditions to the well-equilibrated mean velocity downstream far from the leading edge. The data here shows that the adjustment region appears to be characterized by three stages. The first stage is the flow adjustment at the inlet of the vegetation zone (i.e. in the vicinity of $x = 0$). In this region, streamwise velocity decreases due to the presence of a drag force introduced by the artificial vegetation. The velocity difference between vegetated and non-vegetated areas then produces a free shear layer at the leading edge of the vegetated area. Small-scale vortices appear to evolve along x in this shear layer. The second stage resembles a developing turbulent flow. The shear layer develops and grows sufficiently to penetrate the vegetated area and the width of the mixing layer near the vegetation edge increases and eventually reaches an equilibrium with the vegetation patch size. The third stage is the equilibrium region where the mean transverse velocity distribution becomes approximately homogeneous along the longitudinal direction (i.e.,$\partial u/\partial x = 0$). The longitudinal distance of the entire adjustment region (i.e. from the inlet to the equilibration zone), labeled as X_D, is of practical engineering significance. This distance can inform future designs of the minimum required vegetation length to be used in river management. It is also linked to dynamically similar adjustment distances in forest-edge studies and to equilibration distances following a sudden change in momentum roughness length. In aquatic vegetation studies, Rominger and Nepf (2011) experimentally showed that X_D varies with vegetation density. For low flow-blockage cases ($C_d a B_v < 2$, where $B_v = 0.495$ m is the width of vegetation zone in the transverse direction here, C_d is the drag coefficient and a is roughness density)

$$X_D = (3 \pm 0.3)\left[\frac{2}{C_d a}[1 + (C_d a B_v)^2]\right] \tag{1}$$

while for high flow-blockage, i.e., $C_d a B_v \geqslant 2$,

$$X_D = (7 \pm 0.4)B_v \tag{2}$$

For canopies (vegetated and urban), Belcher et al. (2003) and Coceal and Belcher (2004) indicated that for a sparse vegetation array,

$$X_D = 3\left[\frac{2(1-\phi)}{C_d a}\right] \tag{3}$$

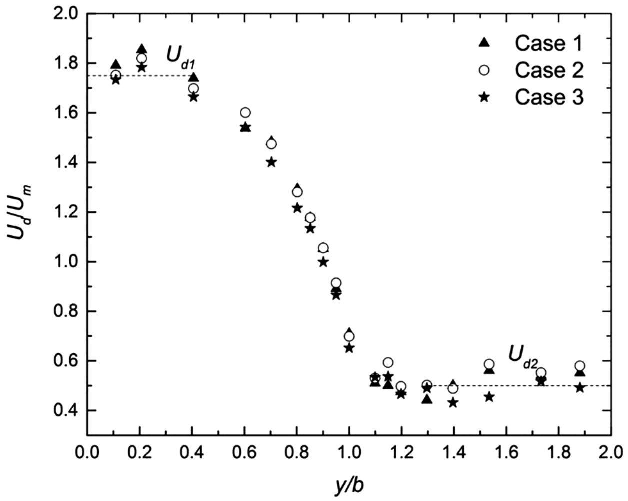

Fig. 5. Transverse distributions of streamwise velocity at the fully equilibrated region. Symbols represent the three experimental conditions summarized in Table 1. U_{d1} and U_{d2} are high- and low-stream velocities.

where ϕ is the solid volume fraction (and $\phi << 1$).

For all three flow configurations summarized in Table 1, $C_d a B_v \approx 0.74 < 2$ (assuming$C_d \approx 1$, an estimate that is to be refined and discussed later on), indicating low vegetation-blockage. Using the aforementioned expressions,$X_D \approx 6.2$m is determined from Rominger and Nepf (2011) whereas $X_D \approx 3.9$m is determined from Belcher et al (2003)'s result. The measured length scale here is $X_{Dmeasured} \approx 4.0$m, in line with Belcher et al. (2003)'s estimates. Fig. 4 shows the mean flow appears to be equilibrated with the vegetation for all three H values when $x/L_{veg} > 0.61$.

Having determined the extent of the transition zone, the vortex sizes impacting the mean flow in the equilibrium zone are now considered. Towards this consideration, the measured transverse distributions of the normalized streamwise velocity in the equilibrium vegetated zone ($x/L_{veg} = 0.61$) are shown in Fig. 5 for all three cases. The canonical shapes of these mean velocity distributions resemble those from classical mixing layer flows (e.g. a hyperbolic tangent). An approximate uniform portion representing the slow flow within the vegetation section (e.g. $y/b > 1.3$) and an approximate uniform portion representing the fast flow outside the vegetated area (e.g. $y/b < 0.5$) are evident for all three cases. The mixing zone between these two near-uniform mean velocity sections defines an effective vortex size and is assumed to originate from Kelvin-Helmholtz instabilities. This vortex size is commonly referred to as the shear length scale in the canopy turbulence literature (Raupach et al., 1996). Despite finding that$C_d a B_v < 2$, the artificial vegetation here appears to be sufficiently dense to introduce an inflection in the mean velocity distribution leading to Kelvin-Helmholtz instabilities (i.e. Rayleigh's inflection-point theorem).

Large momentum exchange occurs in the aforementioned shear layer near the interface between vegetated and non-vegetated areas (i.e. $0.5 < y/b < 1.3$). The momentum thickness θ may be used to measure the effective width of this free shear layer. Its expression is given by

$$\theta = \theta_1 + \theta_2 = \int_{-\infty}^{\infty}\left[\frac{1}{4} - \left(\frac{U_d - \langle U\rangle}{\Delta U}\right)^2\right]dy \tag{4}$$

where θ_1 and θ_2 are the momentum thickness components in vegetated and non-vegetated areas, respectively. Velocity $\langle U\rangle$ is the arithmetic mean of U_{d1} and U_{d2}, namely, $\langle U\rangle = (U_{d1} + U_{d2})/2$. Here, U_{d1} and U_{d2} are the time-averaged velocities in non-vegetated and vegetated areas, respectively (see Fig. 5). The velocity difference ΔU can be calculated from$\Delta U = U_{d1} - U_{d2}$.

The momentum thickness increases rapidly with increasing x and then reaches a constant at about $x/L_{veg} = 0.5$, the same x-position the

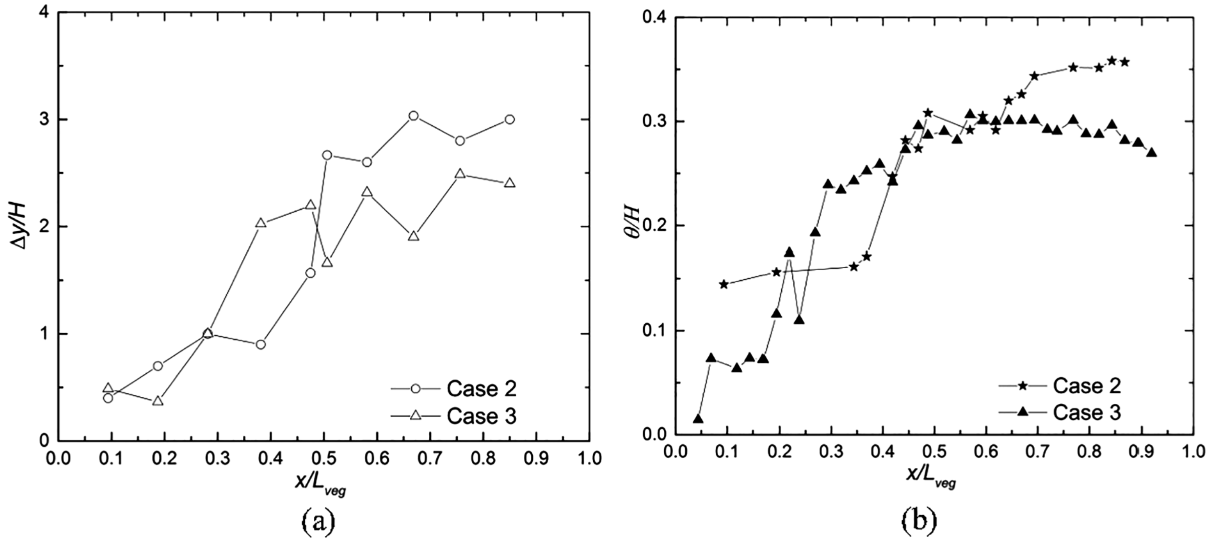

Fig. 6. Momentum thickness θ and mixing layer width Δy growth downstream of the channel for Cases 2 and 3.

mixing layer width nearly achieves independence from x (shown in Fig. 6). This initially rapid development of momentum thickness θ is consistent with other flume experiments (White and Nepf, 2007, 2008). Moreover, the momentum thickness increases significantly with increasing water depth H as evidence here.

After delineating eddy sizes responsible for changes in the shape of the mean velocity distribution with longitudinal distance (i.e. θ or Δy), the properties of eddies that transport momentum are now considered. The transverse distributions of the Reynolds stress in the fully equilibrated zone at $x/L_{veg} = 0.61$ for all three experimental cases are presented in Fig. 7. The first peak of the Reynolds stress that appears at the joint area is evident and is reduced gradually toward the inner side of vegetated and non-vegetated areas. The second peak is inside the vegetated area, and its sign is negative, which is opposite to the sign of the first peak.

For completeness, the measured distribution of $\overline{u'v'}_d$ and U_d are used to estimate the local drag coefficient for the three cases shown in Fig. 8 as a function of y/b. The method of local drag determination and a comparison of these estimates with other estimates (Wang et al., 2015, 2018) in the literature are discussed in the Appendix.

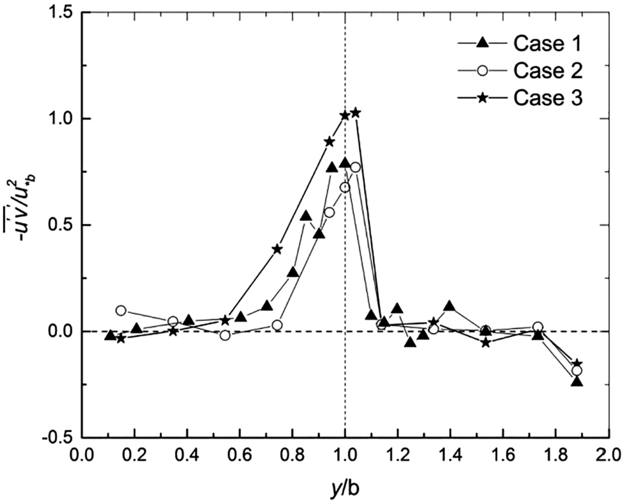

Fig. 7. Transverse distributions of the normalized Reynolds stresses for the fully equilibrated flow (i.e. $x/L_{veg} = 0.61$) for Cases 1–3, respectively. The vertical dashed line delineates the vegetated and non-vegetated zone and the horizontal dashed line indicates no turbulent momentum transport.

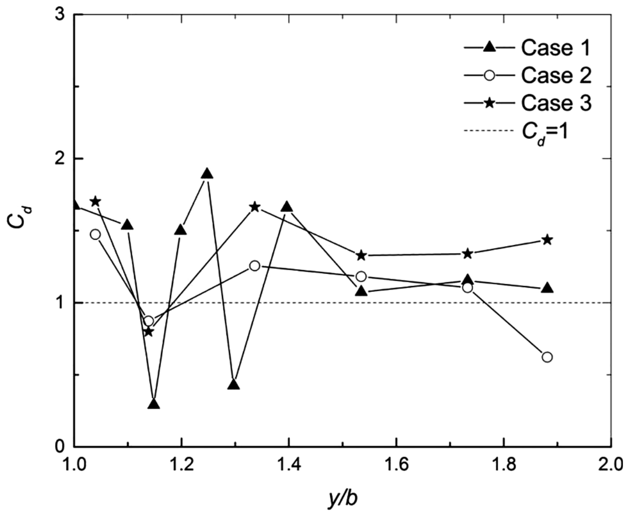

Fig. 8. The variations of the measured 'local' drag coefficient C_d with normalized transverse distance y in the equilibrium region for all three cases. The assumed $C_d = 1$ used in the determination of X_D is also shown as a dashed horizontal line. These estimates here are in agreement with the rod canopy of Poggi et al. (2004).

4.2. Energetic modes and power spectral density analysis

The structure of turbulence within the free shear layer (Fig. 4) formed at the interface between the vegetated and non-vegetated areas is now explored. The coherent vortex structure spreading downstream in this shear layer is the outcome of Kelvin-Helmholtz instability and grows continuously with increasing x until reaching equilibrium ($x/L_{veg} > 0.5$). This vortex type dominates the transverse energy content and momentum transport. Periodic fluctuations in velocity and Reynolds stress at the interface between vegetated and non-vegetated areas are formed by such vortices. Fig. 9 shows a representative time series of the streamwise velocity u, transverse velocity v, and Reynolds stress at $x/L_{veg} = 0.61$, $y/b = 1$ for Case 3. Reynolds stress represents the transverse momentum transport per unit area. The streamwise and transverse velocities are anti-correlated in time indicating strong momentum exchange at this location. Strong sweeps are followed by weak ejections. The fact that quasi-periodicity in velocities and Reynolds stress are similar indicates that a dominant frequency may be defined and determined, which is the main purpose of the spectral analysis

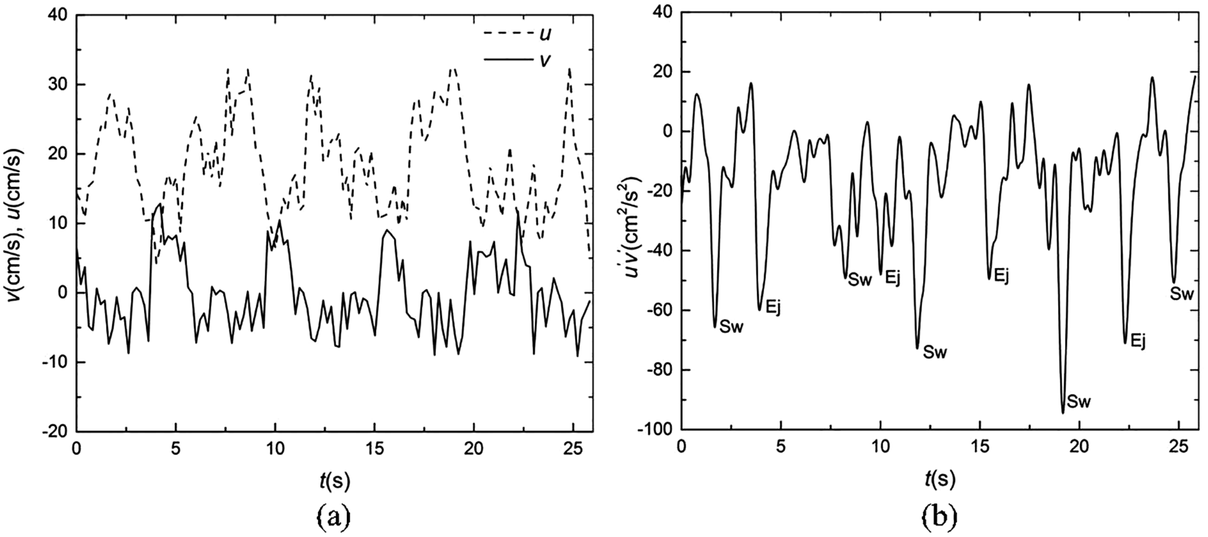

Fig. 9. Sample traces of measured instantaneous streamwise and spanwise turbulent velocity components and Reynolds stress measured at the interface between vegetated and non-vegetated areas ($y/b = 1$) in the fully equilibrated zone ($x/L_{veg} = 0.61$ for Case 3).

next.

The transverse velocity fluctuations at the interface between vegetated and non-vegetated areas are analyzed using spectral analysis. The calculated frequency f is normalized by the local time-averaged velocity $\langle \overline{U} \rangle$ and momentum thickness $\theta(x)$. The spectral analysis used here is based on the Welch method (Welch, 1967) with Hamming type windowing (using Matlab, Mathworks, Natick, MA).

Fig. 10 presents the outcome of the spectral analysis for different downstream positions x/L_{veg}. The peak in the spectral density corresponds to the dominant frequency of coherent vortical structures. At the beginning of the vegetated area $x/L_{veg} < 0.5$, the spectrum exhibits multimodal structures with three or more energetic modes (Fig. 10(a), $x/L_{veg} = 0.34$; 10(b), $x/L_{veg} = 0.19$). The spectrum along the downstream direction evolves to a state exhibiting a single dominant low-frequency mode. For different experimental conditions, the dimensionless frequency $f\theta < \bar{U} > \approx 0.032$ and much of the turbulent energy is explained by this single dominant frequency. The deviation of the spectral peak for each flow condition is small ($\pm$ 0.005).

The two generation mechanisms in the turbulent kinetic energy (TKE) budget are now explored to assess whether mechanical or wake production length scales dominate different flow regions. For this purpose, the shear production (P_s) and wake production (P_w) are computed using (Poggi et al., 2004a,b):

$$P_s = -2\overline{(u'v')}_d \frac{dU_d}{dy} \tag{5}$$

$$P_w = 2C_d a U_d^3 \tag{6}$$

In Fig. 11, the measured depth-averaged P_s and P_w are presented for the equilibrium region along the y direction (i.e. 1-D representation after equilibration). Wake production dominates within the vegetation section whereas shear production dominates at the interface and outside the vegetated areas. This analysis lends support to the duel types of vortices expected here: stem-scale (associated with wakes and stem diameter) and shear-scale vortices (associated with Kelvin-Helmholtz instabilities) that dominate different regions.

The equilibrium zone at $x/L_{veg} = 0.61$ for Case 2 is now used to further investigate the effect of such vortex formation on the flow. A series of instantaneous transverse velocity fluctuation v' was studied at two representative transverse locations ($y/b = 1$ and 1.95) that are close to the outer and inner sides of the vegetated areas where the normalized Reynolds stresses reach unity at $y/b = 1$, and -0.25 at $y/b = 1.95$ near the wall side with vegetation (see Fig. 7).

Fig. 12 presents the variation in the power spectral density of instantaneous transverse velocity fluctuation with frequency f. The dominant frequency at the interface between the vegetated and non-vegetated areas ($y/b = 1$) was determined as $f = 0.13$ Hz whereas the vortex dominant frequency is $f = 0.7$ Hz at the inner side of the vegetated area ($y/b = 1.95$). The normalized Strouhal number (St) is widely used to describe the relation between vortex shedding frequency and an obstacle characteristic length, at least in cases where von Karman streets are spawned from an obstacle or when P_w dominates. The St is given by

$$St = \frac{fL}{U} \tag{7}$$

where f is the vortex shedding frequency, which is the dominant frequency in the spectral analysis, L is a characteristic length of the vortex size, and U is the characteristic velocity (often the approach velocity towards an obstacle is used). Across a wide range of Reynolds number values, the St is constant at 0.21 (Schlichting and Gersten, 1968). This near constant St value was independently shown to explain the peak in the velocity energy spectra within a rigid rod canopy for a wide range of rod densities (Poggi et al., 2004b). At $y/b = 1$ for Case 2 (i.e. at the interface between vegetated and non-vegetated), the f corresponding to the maximum energy content is determined to be approximately 0.13 Hz. When combining this estimate with the characteristic flow (or approach) velocity measured $U = 0.25$ m/s, the constant Strouhal number determines a characteristic vortex length of 0.4 m. This calculated length agrees with the overall width of the vegetated area (=0.495 m). The finding here demonstrates that the vortices at the interface between vegetated and non-vegetated areas are restricted by the width of the artificial vegetation zone even when P_w and P_s are both significant. For another location ($y/b = 1.95$) well-within the vegetated zone, the peak frequency f is 0.68 Hz and U is about 0.1 m/s. Thus, the characteristic length L derived from $St = 0.21$ is 0.03 m, one order of magnitude smaller than the length scale determined at $y/b = 1$. The characteristic vortex length here is reasonably close to the average diameter of the individual vegetation elements. This finding indicates that the vortices within the inner side of vegetated areas are unambiguously generated by P_w consistent with prior results that $P_s < < P_w$ at $y/b = 1.95$. Unlike classical Von Karman streets, the vortices formed by P_w here cannot continue to grow because of collisions with other vegetated elements. Hence, the overall width of the vegetated section sets the maximum vortex size.

Moving beyond the energetic modes, Fig. 12 shows that the

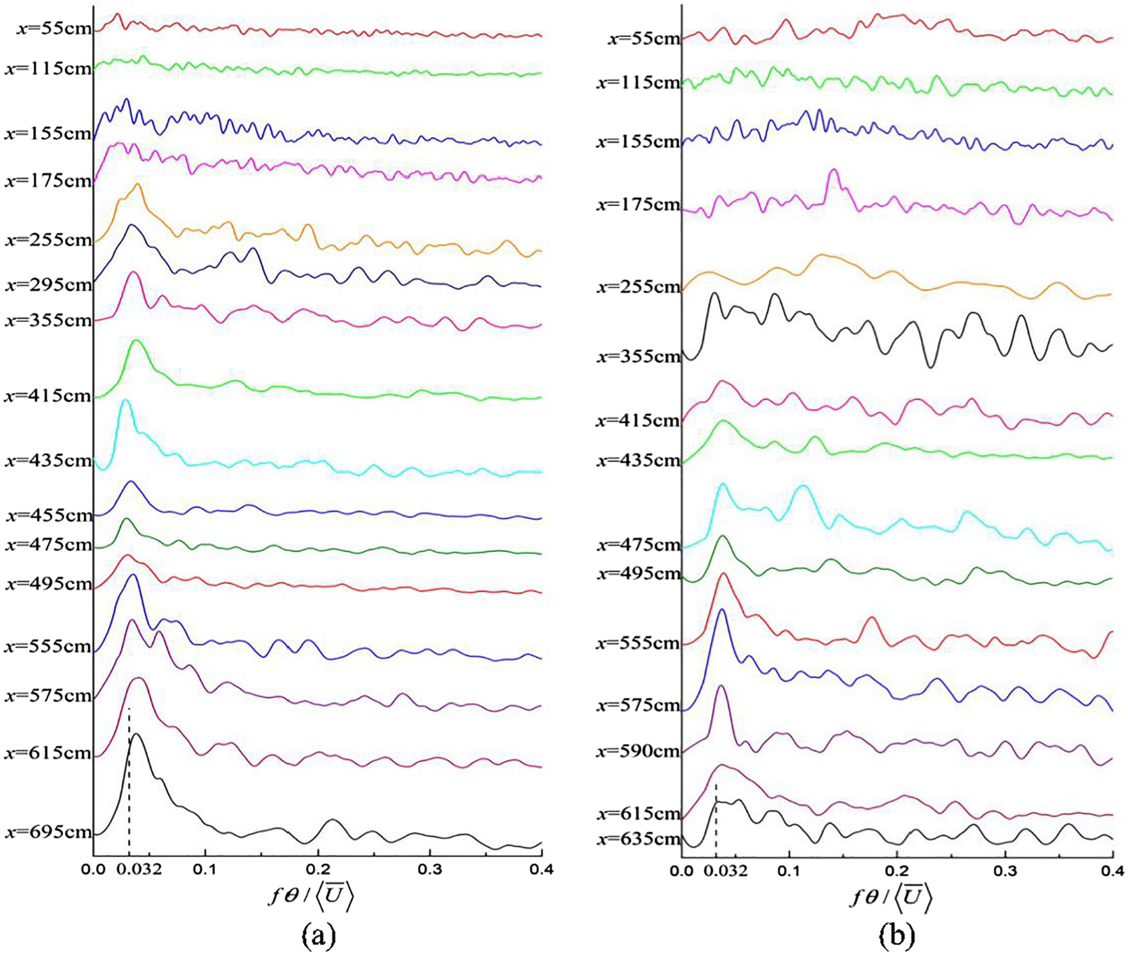

Fig. 10. Power spectral density analysis for different *x*-positions along the channel for Cases 2 and 3.

attenuation rate of the power spectral density at high frequency decays at a rate less steep than the Kolmogorov scaling ($= -5/3$) for locally homogeneous and isotropic turbulence. Attainment of an inertial subrange or local isotropy is not likely at least for the sampling frequency and path-averaging of the ADV instrument used here. The fact that the spectra decay at rates less steep than $-5/3$ is also of significance for LES subgrid schemes. In such schemes, unresolved scales are linked to resolved scales using a scale-dependent eddy viscosity that is derived to match inertial subrange scaling laws. An approximate instrument white-noise appears to dominate frequencies beyond 20 Hz. This white-noise frequency is larger than any of the previously analyzed frequencies associated with characteristic vertical motion. Notwithstanding this noise, the analysis here shows that beyond the energy injection scale, the turbulence cascade does not proceed immediately

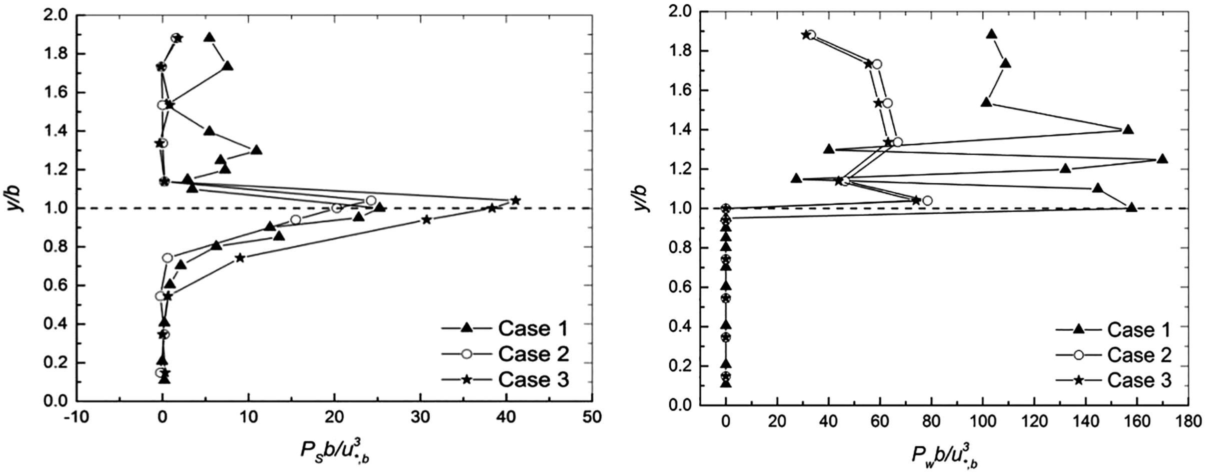

Fig. 11. Transverse distribution of the two production components of the turbulent kinetic energy budget for the equilibrium region ($x/L_{veg} = 0.61$) and for three experimental conditions.

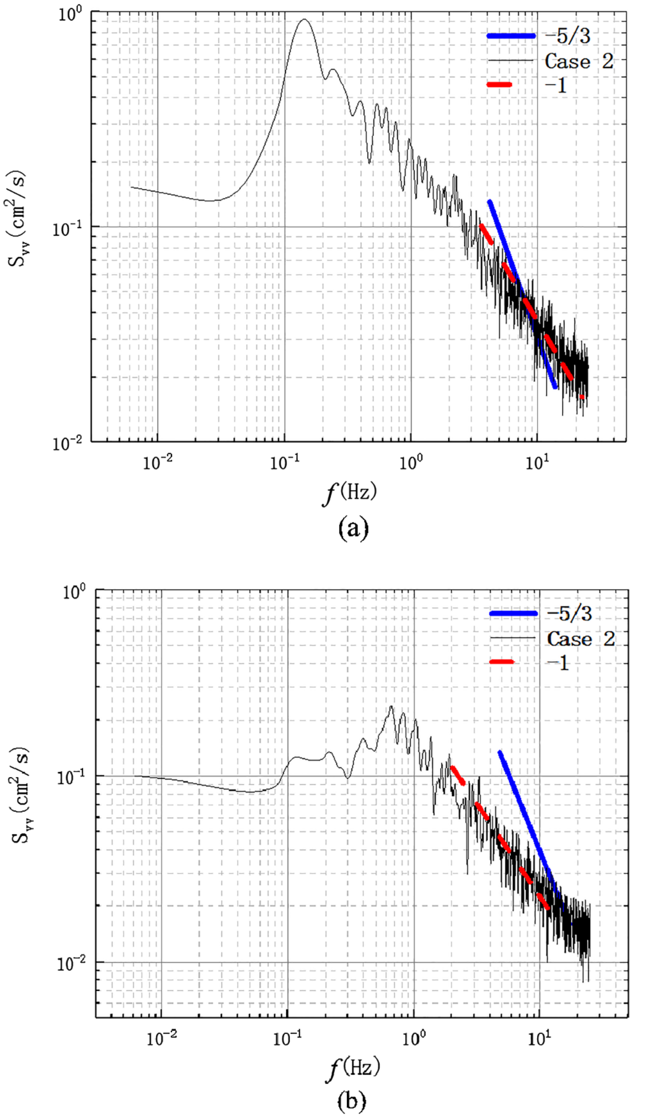

(a)

(b)

Fig. 12. Power spectral density of the spanwise velocity in a cross-sectional plane (x = 490 cm) at two transverse representative locations for Case 2: (a) at the interface between the vegetated and non-vegetated areas (y/b = 1) and (b) at the inner side of the vegetated area (y/b = 1.95). The exponent of the line associated with locally homogeneous and isotropic turbulence predicted from Kolmogorov's theory is − 5/3. The −1 power-law is shown for reference.

following its conventional expectation from locally homogeneous and isotropic turbulence towards finer scales. An inertial subrange may form at frequencies beyond 20 Hz though this cannot be tested here.

While a −5/3 scaling is not attained beyond the energy injection scale with increasing frequency, an approximate f^{-1}power-law scaling seems to emerge from the spectral analysis here. Typically, an f^{-1} power-law scaling in the spectrum (either in f or wavenumber k) is suggestive that the spectrum in this range of eddy sizes is becoming independent of the length scale producing the energy ($=L_E$). Here, L_E may be viewed as the momentum thickness (for Fig. 12a) or the stem diameter (for Fig. 12b) depending on y/b. To speculate on the occurrence of a f^{-1} power-law power-law at scales smaller than L_E, the following dimensional reasoning may be adopted. Because velocity variances are ultimately produced by the gravitational force driving the flow (i.e. $u_{*,b}^2$), then the dimensionless energy spectrum at a large and intermediate range of scales relevant to energy production (i.e. where the majority of the variance lies) may be normalized as (Katul et al., 1995; Katul and Chu, 1998)

$$\frac{S_{vv}(k)}{u_{*,b}^2 L_E} = F_s(kL_E). \tag{8}$$

Here, k is a wavenumber and $F_s(kL_E)$ is a similarity function to be determined as a function of the dimensionless wavenumber (kL_E). If the spectrum of eddies at sizes smaller than L_E become independent of L_E (but they have not cascaded enough to fully attained their near-isotropic state given by Kolmogorov's −5/3 scaling at very large f), then the only way to cancel L_E from both sides of this expression is to set $F_s(kL_E) = A_E/(kL_E)$, whence producing a −1 power-law scaling where A_E is a similarity constant that may vary with H. That is, the −1 power-law scaling is expected to occur at eddy sizes smaller than L_E but much larger than eddy sizes associated with locally homogeneous and isotropic turbulence (and these are not resolved with ADV system here). The range of scales that are described by a near −1 power-law scaling in Fig. 12 appear consistent with the aforementioned analysis. However, this analysis must be only viewed as a plausibility argument to be further explored in future studies (mainly LES studies and laser-doppler anemometry measurements).

4.3. Momentum transfer and quadrant analysis

Quadrant analysis was conducted for the three cases summarized in Table 1 to elucidate the impact of emergent artificial vegetation and H on momentum exchange by vortices that dominate the energy spectra (Antonia, 1981; Wallace, 2016). In quadrant analysis, the Reynolds stress has four types of contributions according to the signs of the instantaneous velocity fluctuations as shown below:

Q1: Quadrant 1, $u' > 0$, $v' > 0$, outward interaction;
Q2: Quadrant 2, $u' < 0$, $v' > 0$, ejection;
Q3: Quadrant 3, $u' < 0$, $v' < 0$, inward interaction;
Q4: Quadrant 4, $u' > 0$, $v' < 0$, sweep.

The four Reynolds stress contributions can also be separated by a hole (instead of zero). The hole is formed by four hyperbolas $|u'v'| = G_0\,|\overline{u'v'}|$, where G_0 is the threshold value (see Fig. 13). Large Reynolds stress contributions in each quadrant can be determined by the threshold value G_0 (Lu and Willmarth, 1973).

The contribution to the Reynolds stress in the Q_i quadrant can be expressed as

$$S_{i,H_0} = \frac{1}{T}\int_0^T C_{i,H_0}(t)u'(t)v'(t)dt \tag{9}$$

where

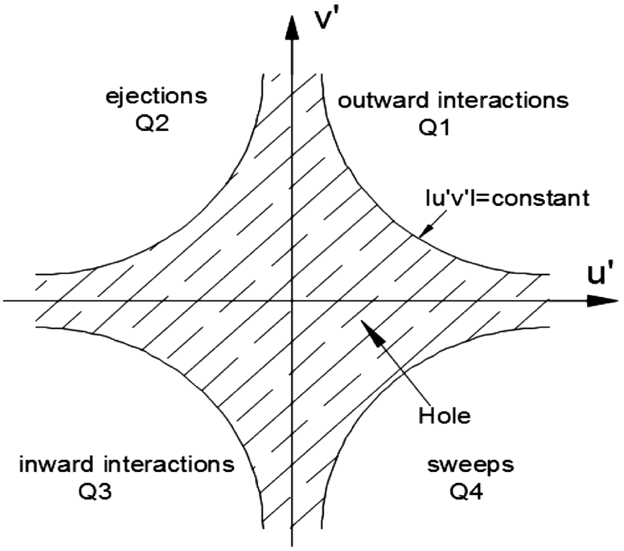

Fig. 13. The sketch of the quadrants responsible for momentum exchange along with the hyperbolic hole.

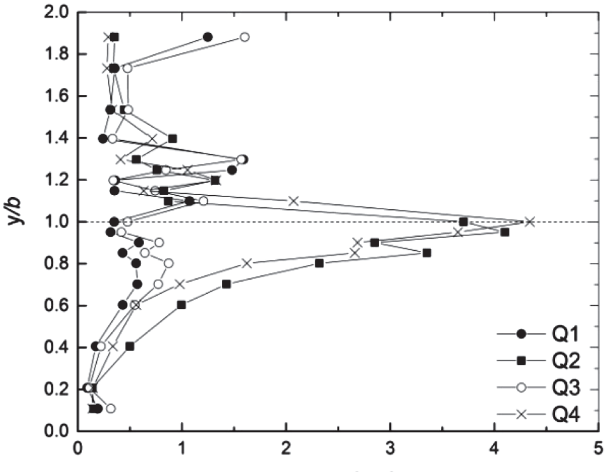

(a) Case 1, $H = 11.5$ cm

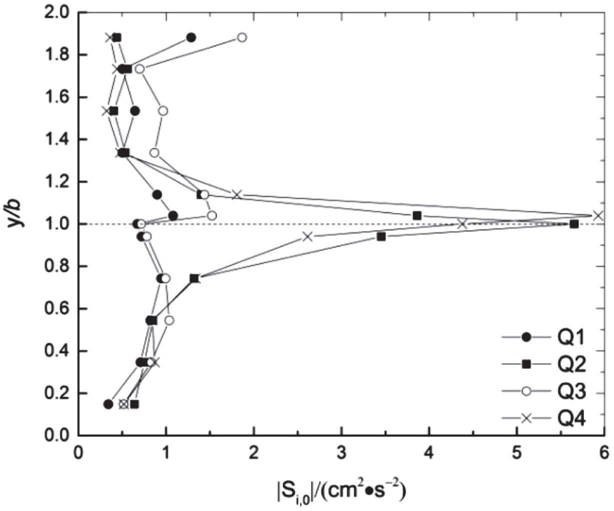

(b) Case 2, $H = 15$ cm

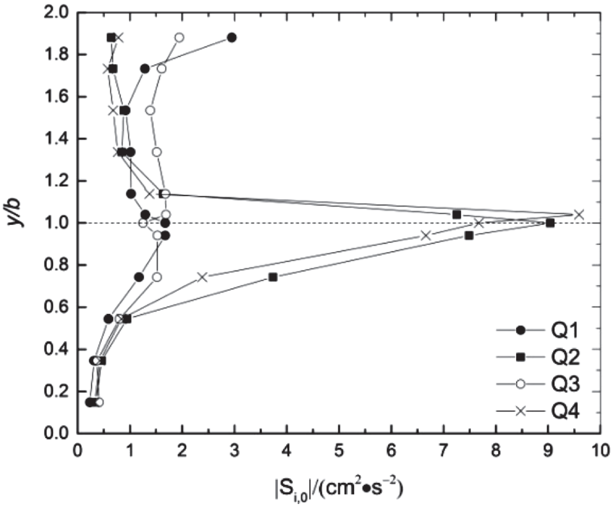

(c) Case 3, $H = 20.5$ cm

Fig. 14. Contributions to Reynolds stresses from each quadrant for Cases 1–3 when the threshold value $G_O = 0$. As before, y is the horizontal distance from the side wall of the non-vegetated area to the measured point, and $|S_{i,0}|$ demonstrates the absolute contribution value to Reynolds stress. The dashed lines indicate the interface between vegetated and non-vegetated areas.

$$C_{i,H_0} = \begin{cases} 1, \ |u'(t)v'(t)| > G_0 \ |\overline{u'v'}| \ and [u'(t), \ v'(t)] in\ the\ quadrant\ Q_i \\ 0, \ otherwise \end{cases} \tag{10}$$

where T is the averaging time, $u'(t)$ and $v'(t)$ are the instantaneous velocity fluctuations in the streamwise and spanwise directions, respectively, and C_{i,H_0} is the average condition.

The transverse distributions of $S_{i,0}$ in the equilibrium zone for $x/L_{veg} = 0.61$ and for each water depth H are presented in Fig. 14. In all the experimental conditions, ejections and sweeps are the main contributions to the turbulent momentum flux at the interface between vegetated and non-vegetated areas. Ejections and sweeps show a decreasing trend from the interface into the vegetated (or non-vegetated) area. Ejections outweigh sweeps outside the vegetated area, and the opposite occurs inside the vegetated area. This turbulence structure is similar to that with submerged rigid vegetation (Poggi et al., 2004a,b; Ghisalberti and Nepf, 2006). Fig. 14 also suggests that outward and inward interactions are dominant contributions near the side wall within the vegetation area ($y/b > 1.9$). The contributions of outward and inward interactions to Reynolds stress are positive, whereas those of sweeps and ejections are negative. Outward and inward interactions are larger than sweeps and injections within the vegetation area of $y/b > 1.9$. Therefore, the signs of Reynolds stress are positive, which is caused by the side-wall effect and opposite to the signs of Reynolds stress at the interface ($y/b \approx 1$).

Fig. 15 demonstrate the development of ratios of sweeps to ejections $|S_{4,H_0}|/|S_{2,H_0}|$ and the ratios of sweeps and ejections to outward and inward interactions $(|S_{4,H_0}| + |S_{2,H_0}|)/(|S_{3,H_0}| + |S_{1,H_0}|)$ across the flume width direction in Case 2 at $x/L_{veg} = 0.61$ (i.e. equilibrium zone). For a bivariate Gaussian distribution, $\frac{|S_{4,H_0}|}{|S_{2,H_0}|} = 1$. Hence, deviations from unity in $\frac{|S_{4,H_0}|}{|S_{2,H_0}|}$ are due to asymmetry in the joint probability density function of the two velocity components analyzed here. The shear contributions of sweeps and ejections are larger than those of outward and inward interactions in the middle of the channel, with this trend reversed inside the vegetated area.

Ratios of sweeps and ejections to outward and inward interactions, $(|S_{4,H_0}| + |S_{2,H_0}|)/(|S_{3,H_0}| + |S_{1,H_0}|)$, are different for various threshold value G_O ranging from 0 to 6 as expected for canopy flows. The shear contribution proportions of sweeps and ejections become significant with increasing G_O near the interface between the vegetated and non-vegetated areas. In Fig. 16, the ratios are roughly the same in vegetated and non-vegetated areas when compared with that near the interface.

Fig. 17 demonstrates how brief but intense vortex-driven events contribute to momentum exchange. With G_O changing from 0 to 6, $S^*(H_0)$ is the proportion of the shear contributions of sweeps and

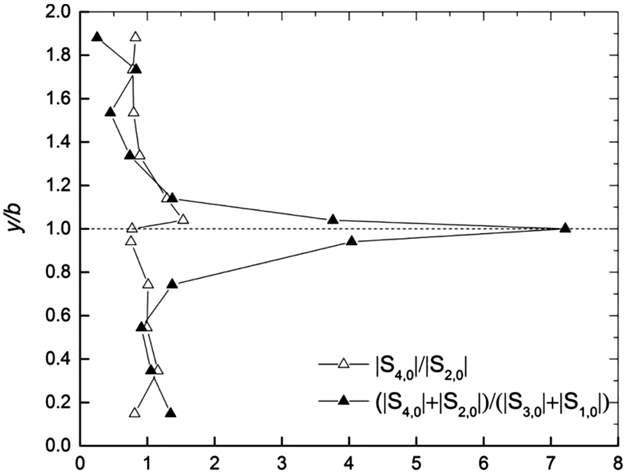

Fig. 15. The ratio of sweeps to ejections and sweeps and ejections to outward and inward interactions in Case 2, $H = 15$ cm.

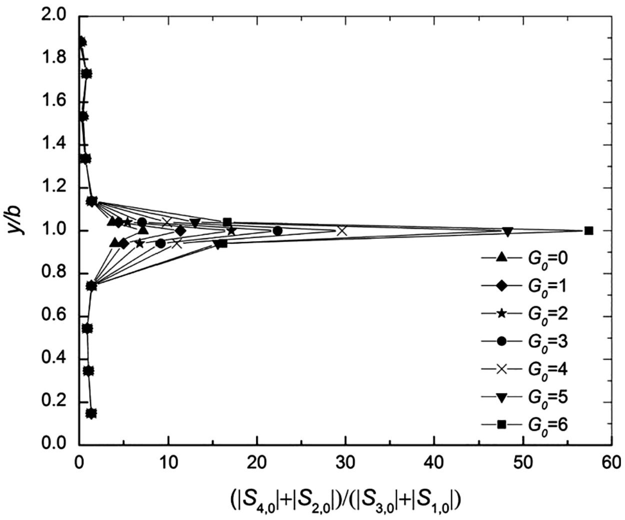

Fig. 16. Changing curvature of the ratio of sweeps and ejections to outward and inward interactions for different thresholds G_O, $H = 15$ cm.

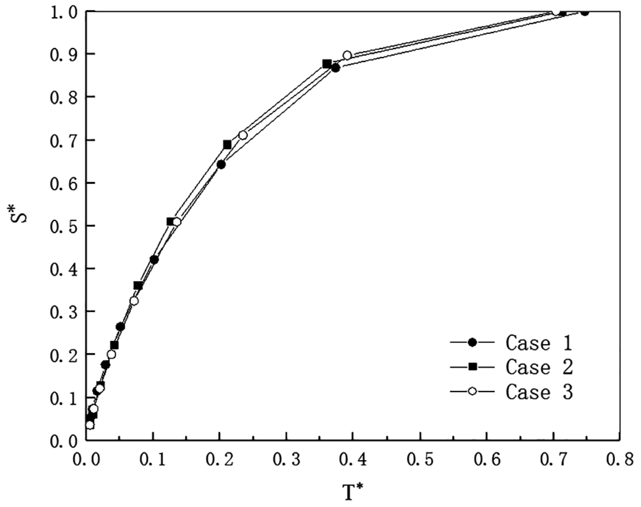

Fig. 17. Development of ejections and sweeps with time fraction T^* for three cases.

ejections larger than the threshold $|H_0\overline{u'v'}|$ at the interface between vegetated and non-vegetated areas, and $T^*(H_0)$ is the ratio of sweeps and ejections to the total duration, as shown

$$S^*(H_0) = (S_{4,H_0} + S_{2,H_0})/(S_{4,0} + S_{2,0}) \tag{11}$$

$$T^*(H_0) = \frac{1}{T}\int_0^T (C_{4,H_0}(t) + C_{2,H_0}(t))dt \tag{12}$$

In all 3 cases, nearly 80% of sweeps and ejections at the interface between the vegetated and non-vegetated areas occur within 30% of the time. When$S^*(0) = 1$, $T^*(0) \approx 0.7$, which indicates that 30% of the total duration is occupied by the inward and outward interactions. This finding is also consistent with other flume experiments on canopy flows (Poggi et al., 2004a; Ghisalberti and Nepf, 2006).

4.4. Linking momentum exchange to spectral and quadrant analyses

A closure model of maximum simplicity is now explored to link the aforementioned vortical sizes to certain features of momentum transport associated with the high ejection-sweep contribution. This model is based on third-order cumulant expansion of the joint *u*-*v* velocity probability density function and was proposed for turbulent flows within and above a rod canopy (Poggi et al. 2004b). The utility of this model is now explored in the context of the vegetation configuration here. The ejection-sweep contribution to momentum exchange was shown to be reasonably summarized by the stress fraction ΔS_0 (Nakagawa and Nezu, 1977; Raupach, 1981) given by

$$\Delta S_0 = \frac{\overline{(u'v')}_d|_4 - \overline{(u'v')}_d|_2}{\overline{(u'v')}_d} \tag{13}$$

where $\overline{(u'v')}_d|_i/\overline{(u'v')}_d$ is the stress fraction in Quadrant i ($i = 1, 2, 3, 4$). A second order RANS closure model prediction for ΔS_0 is derived elsewhere (Poggi et al., 2004b) and given as

$$\Delta S_0 = \frac{-1}{2\sqrt{2\pi}}\frac{q\lambda_1}{\overline{(u'v')}_d}\left[\frac{1}{\sigma_u}\frac{\partial\overline{(u'\mathrm{u}')}_d}{\partial y} - \frac{2}{\sigma_v}\frac{\partial\overline{(u'\mathrm{v}')}_d}{\partial y}\right] \tag{14}$$

where $\sigma_s = \sqrt{\overline{(s's')}_d}$ is the time and depth averaged standard deviation of an arbitrary flow variable s; $q = \sqrt{(u_i'u_i')_d}$ is the turbulent velocity scale; $\lambda_1 = b_1 l_{eff}$ is the length scale, where $b_1 = u_*/q$ is a closure coefficient and l_{eff} is the effective or master length scale of the closure model. The expression of length scale at various horizontal distance y is now derived from the spectral analysis findings. Inside the vegetation area ($y/b > 1.5$), hereafter referred to as region I, the spectral analysis shows that the turbulence generation is mainly produced by stem-scale vortices. Near the interface between the vegetated and non-vegetated areas ($0.5 < y/b < 1.5$), hereafter referred to as region II, the peak of the Reynold stress appears and is explained by shear-scale vortices. For $y/b < 0.5$, hereafter referred to as region III, the length scale is given by a standard boundary-layer length scale. For the synthetic vegetation here, these length scales are

$$\text{region I } l_{eff} = \left(\frac{d}{0.21}\right) \tag{15}$$

$$\text{region II } l_{eff} \approx 0.5\left(l_{BL}(y) + \frac{1}{9}\frac{1}{\langle C_d a\rangle}\right) \tag{16}$$

$$\text{region III } l_{eff} = l_{BL} = k(y - (B_v - \delta_e)) \tag{17}$$

where d is arithmetic mean diameter of the dampers used to construct the artificial vegetation; B_v is the width of the vegetation area; $\langle C_d a\rangle$ is the horizontally-averaged value of a variable $C_d a$ across the width of vegetation area ($=B_v$); $k = 0.4$ is the Von Karman constant; δ_e is the penetration depth and is computed as (Nepf and Vivoni, 2000)

$$\delta_e = \begin{cases} \frac{0.21 \pm 0.03}{C_d a}, & \text{for } C_d a B_v > 0.25 \\ (0.85 \sim 1)B_v, & \text{for } 0.1 < C_d a B_v < 0.25 \end{cases} \tag{18}$$

In Fig. 18, measured stress fraction ΔS_0 obtained from quadrant analysis is compared against predictions from the second-order closure modeledΔS_0. Reasonable agreement between measurements and model calculations are found leading confidence to the determined vortical sizes contributing to ejections and sweeps. It is clear that in the experiments here as well as previous field measurements (Katul and Albertson, 1998; Poggi et al. 2004a), the stress fraction ΔS_0 is a positive value within the vegetation area (i.e. sweeps dominate momentum transfer), while ΔS_0 appears to be negative in the non-vegetated area (i.e. ejections dominate momentum transfer). The good agreement between measured and modeled ΔS_0 demonstrates a novel connection between sweeps and ejections and second-order RANS closure model calculations. It also suggests that asymmetry in momentum exchange (i.e. $\Delta S_0 \neq 0$) may be predicted from the gradients in second-order statistics given by the Eq. (14).

5. Conclusion

Experiments were performed in an open channel partially covered with emergent artificial vegetation. These experiments were partly motivated by the operational use of artificial vegetation to increase water depth and improve navigation in natural rivers. The experiments

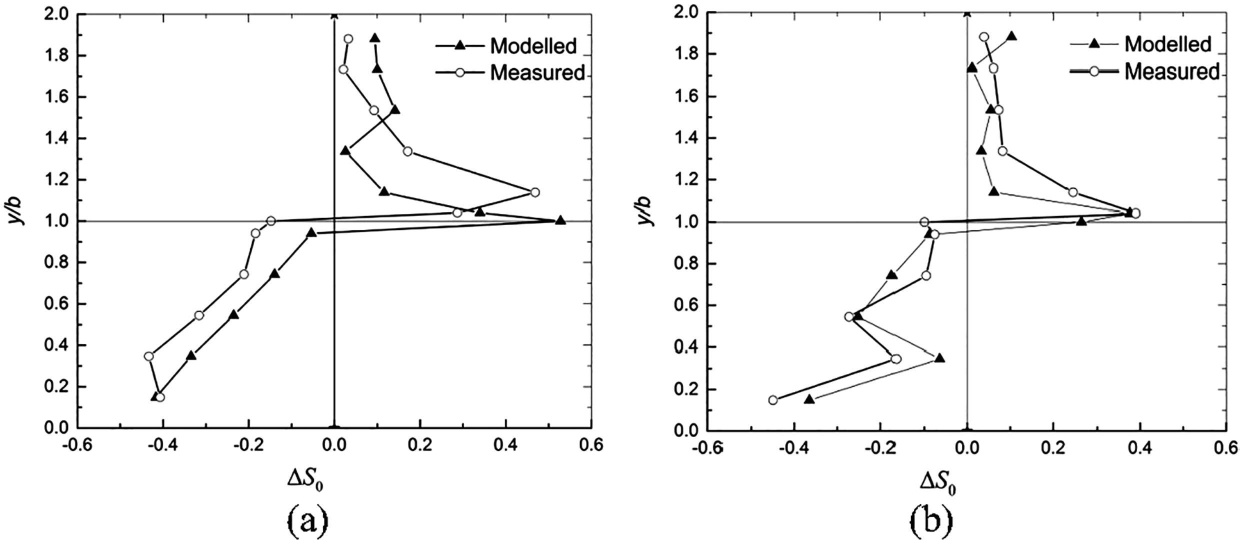

Fig. 18. Comparison between modeled and measured depth-averaged ΔS_0 with lateral distance y/b for two experimental conditions (a) $H = 15$ cm, (b) $H = 20.5$ cm for the equilibrated region.

here differ from conventional canopy flow studies where the flow is uniform and the flow statistics vary along the vertical direction. The vegetation cover employed here is emergent and occupies part of the width and length of the channel. Such canopy placement results in flow statistics that mainly vary in the longitudinal and transverse directions, at least for the purposes of momentum exchange and resistance to flow. The experiments here point to the following:

(1) Flow velocity through the vegetation area is significantly reduced but remains finite, which indicates that the vegetation can increase flow resistance and then enhance overall water depth.

(2) The presence of vegetated and non-vegetated areas leads to an inflection point in the mean velocity along the transverse direction analogous to its well-studied vertical direction counterpart. The mean velocity distribution adjusts along the longitudinal direction and eventually stabilizes to a quasi-equilibrium shape in the transverse direction given by the X_D. The equilibrium transverse Reynolds stress distribution reaches a maximum at the interface between vegetated and non-vegetated areas and is appreciably reduced towards the side-walls of the channel. Negative Reynolds stress was measured on the inner side of the vegetated area, which is consistent with the result of the quadrant analysis that inward and outward interactions are the dominant contributors to Reynolds stress in the same zone analyzed.

(3) The trends of the mixing layer thickness along the main streamwise direction are the same as that of the momentum thickness. These length scales grow at first and then stabilize to an equilibrium value. The inflection in the transverse mean velocity leads to coherent vortex structures that resemble plane mixing layers. In the shear layer, the dominant frequency of this vortex was determined from spectral analysis. When this frequency is normalized by the equilibrated momentum thickness and mean velocity, an invariant value of 0.032 emerges for various water depths. Shear-scale and stem-scale vortices were also determined from spectral analysis and independently supported from TKE production terms. The former appears near the interface between vegetated and non-vegetated zones, whereas the latter emerges on the inner side of the vegetation area.

(4) Sweeps and ejections are major contributions to the Reynolds stress near the interface between vegetated and non-vegetated areas, whereas inward and outward interactions are dominant contributions on the inner side of the vegetation area. Sweeps are more significant than ejections within the vegetated area, with the relation reversed outside the vegetated area. The characteristics of sweeps and ejections are brief and intense. Some 80% of the momentum transport occurs within 30% of the averaging interval. This finding is insensitive to water depth variations.

(5) The work here also offers a blueprint of how to connect the spectral analysis, the conditional sampling and quadrant analysis, and second-order closure modeling. In particular, it was shown that ΔS_0, which measures the relative contributions of sweeps and ejections to momentum transport can be predicted from the canonical length scales in each region and transverse gradients of second moments only. Hence, the work here shows that the asymmetry in ΔS_0 (recall that$\Delta S_0 = 0$ for a Gaussian distribution) may be linked to the large gradients in second-moments due to the presence of vegetation.

Acknowledgments

Wen-Xin Huai and Jiao Zhang acknowledge support from the National Natural Science Foundation of China (Grant Nos. 51439007, 11672213 and 11872285). G. Katul acknowledges support from the U.S. National Science Foundation (NSF-EAR-1344703, NSF-AGS-1644382, and NSF- IOS-1754893). Wei-Jie Wang acknowledges support from the National Natural Science Foundation of China (Grant No. 51809286), China Postdoctoral Science Foundation (grant No. 2017 M610949 and 2018T110122) and the IWHR Research and Development Support Program of China (WE0145B062019). We thank editors and anonymous reviewers for their helpful comments on this paper.

Appendix:

Estimation of the drag coefficient from the measured mean velocity and stress profiles

The drag coefficient of the artificial vegetation is a key parameter in the mean momentum equation and can be evaluated through the components of the mean momentum balance in the 'equilibrated section', given by (Poggi et al. 2004a; Shiono and Knight, 1991)

Table A1
Spatial averaged drag coefficient for three runs.

No.	$< Re_d >$	$\langle C_d \rangle$
Case 1	2719	1.21
Case 2	3304	1.09
Case 3	3134	1.38

$$\frac{\partial H\overline{(u'v')}_d}{\partial y} + gHS_o - \frac{f}{8}U_d^2 - \frac{1}{2}C_{d\langle z\rangle}aHU_d^2 = 0 \tag{A1}$$

which is suitable for steady uniform flow. In this equation a is frontal area index, namely $a = nd$, in which n is vegetation density and d is frontal width of vegetation (diameter here), $C_{D\langle z\rangle}$ denotes depth-averaged coefficient varies with y, and can be used to obtain spatial-averaged value as

$$\langle C_d \rangle = \frac{1}{B}\int_{y=0}^{B} C_{d\langle z\rangle}dy \tag{A2}$$

where $\langle C_d >$ denotes spatial averaged drag coefficient, and element Reynolds number $Re_d = Ud/\nu$, details were shown in Table A1.

In Eq. (A1), f is a ground and side friction coefficient and can be determined by (Rameshwaran and Shiono, 2007):

$$\begin{cases} f = \left[-2\log\left(\frac{3.02\nu}{\sqrt{128gH^3s}} + \frac{k_s}{\Phi H}\right)\right]^{-2} \\ k_s = (8.25n_b\sqrt{g})^6 \end{cases} \tag{A3}$$

where n_b is the manning coefficient of the channel; ν is the flow kinematic viscosity; the values of $\Phi = 1.2$ in the vegetated area.

Differences between the C_d derived here for the synthetic vegetation and prior vegetated studies is further explored in this appendix. For isolated cylinders, the drag coefficient primarily varies with the element Reynolds number $Re_d = Ud/\nu$ and can be approximated by Cheng (2013)

$$\langle C_{d-isolated} \rangle = 11\mathrm{Re}_d^{-0.75} + 0.9\Gamma_1(\mathrm{Re}_d) + 1.2\Gamma_2(\mathrm{Re}_d) \tag{A4}$$

where

$$\Gamma_1(\mathrm{Re}_d) = 1 - \exp\left(-\frac{1000}{\mathrm{Re}_d}\right) \tag{A5}$$

$$\Gamma_2(\mathrm{Re}_d) = 1 - \exp\left[-\left(\frac{\mathrm{Re}_d}{4500}\right)^{0.7}\right] \tag{A6}$$

For an array of vegetation, Cheng and Nguyen (2010) reported a monotonic decline in $\langle C_d \rangle$ but with an increasing vegetation-related Reynolds number (Re_v) for canopies composed of cylinders, as

$$\langle C_{d-cheng} \rangle = 50(\mathrm{Re}_v)^{-0.43} + 0.7\left[1 - \exp\left(-\frac{\mathrm{Re}_v}{15000}\right)\right] \tag{A7}$$

where Re_v is a vegetation-related Reynolds calculated from

$$\mathrm{Re}_v = \frac{uR_v}{\nu} \tag{A8}$$

where

$$R_v = \frac{\pi D}{4}\frac{1-\phi_{veg}}{\phi_{veg}} \tag{A9}$$

For a vegetation array subjected to non-uniform flow, Wang et al. (2015) and Wang et al. (2018) found that the volume-averaged $\langle C_d \rangle$ across the entire vegetation zone declines with Re_v. Their data can be reasonably summarized by (Wang et al., 2018)

$$\langle C_{d-wang} \rangle = E_{n,veg}\exp[-4.14\ln(\mathrm{Re}_v) + 31.80] \tag{A10}$$

and where $E_{n,veg} = 2(1-\phi)\frac{L_xL_y}{DL_{veg}}$ (A11)

Here, $L_x = 0.2$ m, $L_y = 0.1$ m is the distance between two nearby vegetated elements in the longitudinal and transverse directions. The L_{veg} is set at 0.77 m (the value from the experiments in Wang et al., 2018) as a constant parameter here.

The $\langle C_d \rangle$ derived from Eq. A2 is now compared with the differernt methods in Fig. A1. The measured $\langle C_d \rangle$ variations in the range of 1–1.5, appear to exhibit a trend similar to the Cheng and Nguyen (2010)'s study. Moreover, the variations in C_d are larger than those reported for isolated cylinders or spatial-averaged of Wang et al. (2018) 's study.

Declaration of interests

None.

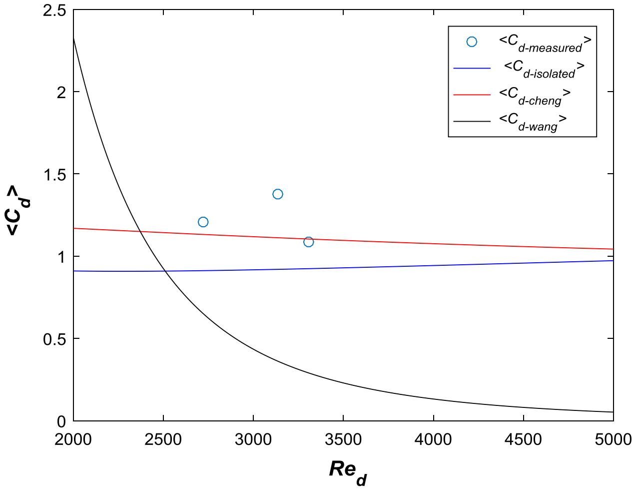

Fig. A1. Comparison of the spatial-averaged drag coefficient using different methods as a function of the element-based Reynolds number.

References

Allmendinger, N.E., Pizzuto, J., Potter, N., Johnson, T., Hession, W.C., 2005. The influence of riparian vegetation on stream width, Eastern Pennsylvania, USA. Geol. Soc. Am. Bull. 117 (1–2), 229–243. https://doi.org/10.1130/B25447.1.

Anderson, B., Rutherfurd, I., Western, A.W., 2006. An analysis of the influence of riparian vegetation on the propagation of flood waves. Environ. Modell. Software 21, 1290–1296.

Antonia, R.A., 1981. Conditional sampling in turbulence measurements. Ann. Rev. Fluid Mechan. 13, 131–156.

Belcher, S.E., Jerram, N., Hunt, J.C.R., 2003. Adjustment of a turbulent boundary layer to a canopy of roughness elements. J. Fluid Mechan. 488 (488), 369–398.

Camporeale, C., Perucca, E., Ridolfi, L., Gurnell, A.M., 2013. Modeling the interactions between river morphodynamics and riparian vegetation. Rev. Geophys. 51 (3), 379–414.

Cheng, N.S., 2013. Calculation of drag coefficient for arrays of emergent circular cylinders with pseudofluid model. J. Hydraul. Eng. 139 (6), 602–611.

Cheng, N.S., Nguyen, H.T., 2010. Hydraulic radius for evaluating resistance induced by simulated emergent vegetation in open channel flows. J. Hydraul. Eng. 137 (9), 995–1004.

Coceal, O., Belcher, S.E., 2004. A canopy model of mean winds through urban areas. Quart. J. R. Meteorol. Soc. 130 (599), 1349–1372.

Dunn, C., Lopez F., Garcia M., 1996. Mean flow and turbulence in a laboratory channel with simulated vegetation, Hydraul. Eng. Ser., 51, Univ. of Ill., Urbana.

Ghisalberti, M., Nepf, H.M., 2002. Mixing layers and coherent structures in vegetated aquatic flows. J. Geophys. Res. Oceans 107 (C2 3), 1–11.

Ghisalberti, M., Nepf, H.M., 2006. The structure of the shear layer in flows over rigid and flexible canopies. Environ. Fluid Mechan. 6 (3), 277–301.

Ghisalberti, M., Nepf, H.M., 2009. Shallow flows over a permeable medium: the hydrodynamics of submerged aquatic canopies. Transp. Porous Media 78 (2), 309–326.

Ho, C.M., Huerre, P., 1984. Perturbed free shear layers. Ann. Rev. Fluid Mechan. 16 (1), 365–422.

Hopkinson, L.C., 2014. Flow through Vegetation Patches with Multiple Layers: A Quadrant Analysis. World Environmental and Water Resources Congress 2012 @ Crossing Boundaries. ASCE 2012, 1406–1415.

Huai, W., Shi, H., Song, S., Ni, S., 2018. A simplified method for estimating the lo-ngitudinal dispersion coefficient in ecological channels with vegetation. Ecol. Indicat. 92, 91–98.

Järvelä, J., 2005. Effect of submerged flexible vegetation on flow structure and resistance. J. Hydrol. 307 (1), 233–241.

Katul, G.G., Chu, C.R., 1998. A theoretical and experimental investigation of energy-containing scales in the dynamic sublayer of boundary-layer flows. Bound.-Layer Meteorol. 86 (2), 279–312.

Katul, G.G., Chu, C.R., Albertson, J.D., Parlange, M.B., 1995. The low-wavenumber spectral characteristics of velocity and temperature in the atmospheric surface layer. J. Geophys. Res. 100, 14243–14255.

Katul, G.G., Albertson, J.D., 1998. An investigation of higher order closure models for a forested canopy. Bound.-Layer Meteorol. 89, 47–74.

Katul, G.G., Mahrt, L., Poggi, D., Sanz, C., 2004. One- and two-equation models for canopy turbulence. Bound.-Layer Meteorol. 113 (1), 81–109.

Katul, G.G., Wiberg, P., Albertson, J., Hornberger, G., 2002. A mixing layer theory for flow resistance in shallow streams. Water Resour. Res. 38 (11) 32 31.

Kubrak, E., Kubrak, J., Rowiński, P.M., 2008. Vertical velocity distributions through and above submerged, flexible vegetation. Hydrol. Sci. J. 53 (4), 905–920.

Lu, S.S., Willmarth, W.W., 1973. Measurements of the structure of the Reynolds stress in a turbulent boundary layer. J. Fluid Mechan. 60 (3), 481–511.

Maltese, A., Cox, E., Folkard, A.M., Ciraolo, G., Loggia, G.L., Lombardo, G., 2007. Laboratory measurements of flow and turbulence in discontinuous distributions of ligulate seagrass. J. Hydraulic Eng. 133 (7), 750–760.

Murota, A., Fukuhara, T., Sato, M., 1984. Turbulence structure in vegetated open channel flows. J. Hydrosci. Hydraul. Eng. 2 (1), 47–61.

Nakagawa, H., Nezu, I., 1977. Prediction of the contributions to the Reynolds stress from bursting events in open-channel flows. J. Fluid Mechan. 80 (1), 99–128.

Nepf, H.M., Vivoni, E.R., 2000. Flow structure in depth-limited, vegetated flow. J. Geophys. Res. Oceans 105 (C12), 28547–28557.

Nezu, I., Sanjou, M., 2009. Turbulence structure and coherent motion in vegetated canopy open-channel flows. J. Hydro-Environ. Res. 2 (2), 62–90.

Poggi, D., Porporato, A., Ridolfi, L., Albertson, J.D., Katul, G.G., 2004a. The effect of vegetation density on canopy sub-layer turbulence. Bound.-Layer Meteorol. 111 (3), 565–587.

Poggi, D., Katul, G.G., Albertson, J.D., 2004b. Momentum transfer and turbulent kinetic energy budgets within a dense model canopy. Bound.-Layer Meteorol. 111 (3), 589–614.

Pope, S.B., 2000. Turbulent Flows. Cambridge Univ. Press, New York.

Rabkova, E.K., Garanina, E.V., 2001. Distribution of averaged local velocities in an open turbulent flow. Water Resour. 28 (5), 577–580.

Rameshwaran, P., Shiono, K., 2007. Quasi two-dimensional model for straight overbank flows through emergent. J. Hydraul. Res. 45 (3), 302–315.

Raupach, M.R., 1981. Conditional statistics of reynolds stress in rough-wall and smooth-wall turbulent boundary layers. J. Fluid Mechan. 108, 363–382.

Raupach, M.R., Thom, A.S., 1981. Turbulence in and above plant canopies. Annu. Rev. Fluid Mech. 13 (1), 97–129.

Raupach, M.R., Finnigan, J.J., Brunet, Y., 1996. Coherent eddies and turbulence in vegetation canopies: The mixing-layer analogy. Bound.-Layer Meteorol. 78, 351–382.

Righetti, M., 2008. Flow analysis in a channel with flexible vegetation using double-averaging method. Acta Geophys. 56 (3), 801–823.

Rominger, J.T., Nepf, H.M., 2011. Flow adjustment and interior flow associated with a rectangular porous obstruction. J. Fluid Mechan. 680 (680), 636–659.

Schlichting, H., Gersten, K., 1968. Boundary-Layer Theory. McGraw-Hill, New York, pp. 681.

Shiono, K., Knight, D.W., 1991. Turbulent open-channel flows with variable depth across the channel. J. Fluid Mechan. 222, 617–646.

Termini, D., 2015. Flexible vegetation behavior and effects on flow conveyance: experimental observations. Int. J. River Basin Manage. 13 (4), 401–411.

Vivoni, E.R., 1998. Turbulence Structure of a Model Seagrass Meadow. M.S. thesis. Mass. Inst. of Technol, Cambridge.

Wallace, J.M., 2016. Quadrant analysis in turbulence research: History and evolution. Ann. Rev. Fluid Mechan. 48, 131–158.

Wang, W.J., Huai, W.X., Thompson, S., Katul, G.G., 2015. Steady nonuniform shallow flow within emergent vegetation. Water Resour. Res. 51 (12), 10047–10064.

Wang, W.J., Huai, W.X., Thompson, S., Peng, W.Q., Katul, G.G., 2018. Drag coefficient estimation using flume experiments in shallow non-uniform water flow within emergent vegetation during rainfall. Ecol. Indicat. 92, 367–378.

Welch, P.D., 1967. The use of Fast Fourier Transform for the estimation of power spectra: a method based on time averaging over short, modified periodograms. IEEE Trans. Audio Electroacoust. 15 (2), 70–73.

White, B.L., Nepf, H.M., 2007. Shear instability and coherent structures in shallow flow adjacent to a porous layer. J. Fluid Mechan. 593 (593), 1–32.

White, B.L., Nepf, H.M., 2008. A vortex-based model of velocity and shear stress in a partially vegetated shallow channel. Water Resour. Res. 44, W01412.

Zdankus, N., Punys, P., Martinaitis, E., Zdankus, T., 2016. Lowland river flow control by an artificial water plant system. River Res. Applicat. 32 (6), 1382–1391.